CHEMISTRY

Deconvolution of metal apportionment in bulk metal-organic frameworks

Jun Xu[1,2]*†, Xingwu Liu[3,4]†, Xingchen Liu[3,5]†, Tao Yan[3,4,5]†, Hongliu Wan[3,4,5], Zhi Cao[3,4,5]*, Jeffrey A. Reimer[2,6]*

We report a general route to decipher the apportionment of metal ions in bulk metal-organic frameworks (MOFs) by solid-state nuclear magnetic resonance spectroscopy. We demonstrate this route in $Mg_{1-x}Ni_x$-MOF-74, where we uncover all eight possible atomic-scale Mg/Ni arrangements through identification and quantification of the distinct chemical environments of ^{13}C-labeled carboxylates as a function of the Ni content. Here, we use magnetic susceptibility, bond pathway, and density functional theory calculations to identify local metal bonding configurations. The results refute the notion of random apportionment from solution synthesis; rather, we reveal that only two of eight Mg/Ni arrangements are preferred in the Ni-incorporated MOFs. These preferred structural arrangements manifest themselves in macroscopic adsorption phenomena as illustrated by CO/CO_2 breakthrough curves. We envision that this nondestructive methodology can be further applied to analyze bulk assembly of other mixed-metal MOFs, greatly extending the knowledge on structure-property relationships of MOFs and their derived materials.

INTRODUCTION

The preparation of bulk chemicals via mixing precursors in the liquid phase, followed by heating to produce solids, has been well established since antiquity. The resulting solid product is presumed to have stoichiometry simply related to the solution mixtures, e.g., ions distributed randomly throughout the product. The apportionment of structural elements, however, remains an important question in materials science, as the spatial distribution of components in a solid may well affect properties. The question of apportionment is particularly important in the chemical synthesis of metal-organic frameworks (MOFs), where properties can be facilely tuned by introducing heterogeneity into MOFs using mixed-organic linkers (the multivariate MOFs) or mixed-metal ions (the mixed-metal MOFs) (1–3). The organic linkers in multivariate MOFs have been apportioned by nondestructive solid-state nuclear magnetic resonance (SSNMR) spectroscopy in combination with computational screening (4). The order of linkers with identical chemical structure but different configurations in MOF superstructure is resolved in a similar way (5). A recent SSNMR work uncovers the arrangement of metal ions within trimers of MIL-100(Al,Fe) (6). However, the experimental identification of metal apportionment is much more challenging for MOFs with infinite number of metal permutations, and the only successful attempt to date was accomplished from destructive atom probe tomography study of mixed-metal MOF-74 single crystals (7). Here, we demonstrate that SSNMR reveals atomic-scale metal apportionment within bulk mixed-metal MOFs as evidenced by our analyses of $Mg_{1-x}Ni_x$-MOF-74 (x = 0.00 to 1.00). Assignment of individual NMR peaks to specific local bonding configurations proceeds from ferromagnetic (FM) and antiferromagnetic (AFM) susceptibility measurements, bond pathway analyses, and density functional theory (DFT) calculations. We illustrate that these structural details are responsible for the superior performances of mixed-metal MOFs compared to their monometallic counterparts in applications, such as the adsorption of industrially important CO gas. We envision that this proposed SSNMR strategy (Fig. 1) will enrich the current knowledge and complement methodology in design, synthesis, characterization, and application of new functional materials.

RESULTS

SSNMR measurements

We used a one-pot approach (8) to synthesize phase pure $Mg_{1-x}Ni_x$-MOF-74 samples (fig. S1), which are constructed by infinite metal-oxygen chains and 2,5-dihydroxyterephthalate (DHTP) linkers interconnected via oxygen atoms (fig. S2), where methanol exchange was used before subsequent structural studies (9). The metal apportionment of mixed-metal MOFs at macroscopic and microscopic length scales (Fig. 2) is typically measured by elemental analysis such as inductively coupled plasma optical emission spectroscopy (ICP-OES) and energy-dispersive x-ray spectroscopy (EDS) (8), respectively. We performed these two characterizations accordingly. The results reveal homogenous Mg/Ni apportionment at macroscopic (table S1) and microscopic (figs. S3 to S11 and table S2) length scales but do not assess apportionment at atomic scale. We surmise that SSNMR measurements will identify Mg/Ni apportionment at atomic scale via the distinguishable ^{13}C chemical shifts engendered from binding of carboxylate to paramagnetic Ni^{2+} ions (S = 1), which are fingerprints of Mg/Ni stoichiometry and sequence along metal-oxygen chains (Fig. 1) (10). The chemical shift changes induced by paramagnetic ions have been shown effective in probing the local bonding configuration of atoms proximate to metal ions in oxides and hydroxides (11–13), as well as SSNMR studies of monometallic MOFs (14–21). Here, we ^{13}C-labeled carboxylate groups of
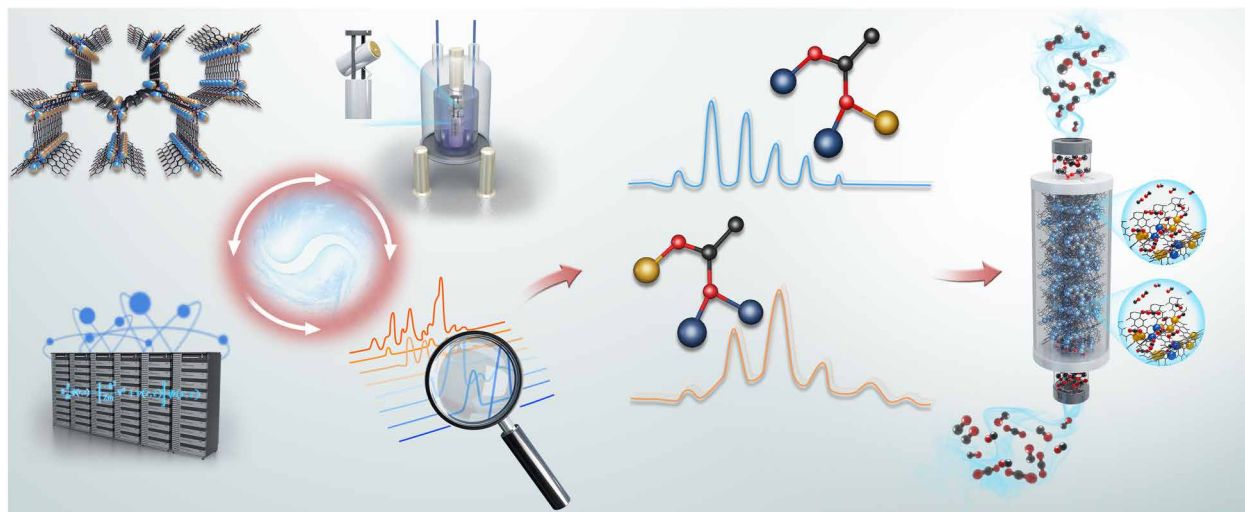
Fig. 1. Schematic illustration of uncovering the atomic-scale Mg/Ni apportionment in bulk Mg$_{1-x}$Ni$_x$-MOF-74 samples by SSNMR and using this information to understand their macroscopic properties.
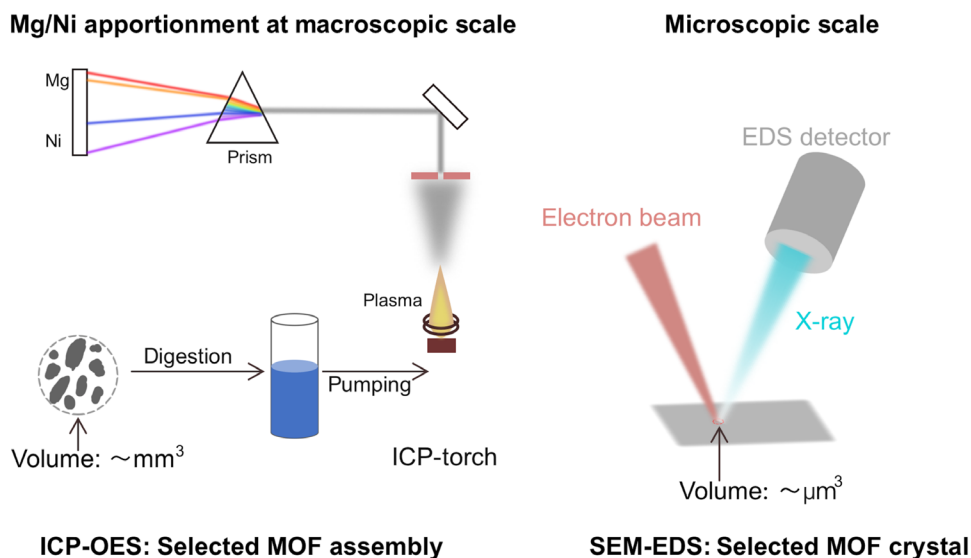

Fig. 2. Schematic illustration of measuring Mg/Ni apportionment in Mg$_{1-x}$Ni$_x$-MOF-74 at macroscopic and microscopic length scales. SEM, scanning electron microscopy.

Mg$_{1-x}$Ni$_x$-MOF-74 samples (fig. S12) to visualize the effects of paramagnetic Ni^{2+} ions so as to probe the spatial distribution of metal ions. In particular, we take advantage of isotopic enrichment at the carboxylate groups [98 atomic % (at %) ^{13}C] to provide an enhancement of ~90 in sensitivity of carboxylate over natural abundance (1.07 at %) ^{13}C associated with the remaining carbons of DHTP.

In particular, we relied on ^{13}C magic angle spinning (MAS) NMR to analyze the chemical shifts of carboxylate moieties, thus discerning the Mg/Ni apportionment. As shown in Fig. 3A and fig. S13, the ^{13}C NMR spectrum of (pure magnesium) Mg-MOF-74 features a narrow peak at 175 parts per million (ppm) (22). The incorporation of Ni into Mg-MOF-74 results in a set of additional four narrow peaks at 230, 210, 203, and 144 ppm and another class of three broad peaks centered at 817, 715, and 197 ppm. The identification of five narrow and three broad peaks was further confirmed by deconvoluting NMR

spectra (figs. S14 to S18) and repeating SSNMR measurements and analyses at a different MAS frequency (figs. S19 to S24). The correlation of these peaks with solvent molecules (methanol) trapped in MOF channels is excluded (fig. S25). These preliminary observations unambiguously verify that our approach is very sensitive to the changes in the Ni content, and multiple local chemical environments of carboxylate can be probed and distinguished.

Atomic-scale metal apportionment

Zooming into the local chemical environments of carboxylate, each carboxylate is bonded to three metal ions via one μ_1-O and one μ_2-O, and the three metal ions are characterized by a 3$_1$ skew axis parallel to the crystallographic c axis (the sequence of three metal ions is hereafter referred to as the Mg/Ni arrangement; Fig. 3B). Together, there are eight possible arrangements (from μ_1-O to μ_2-O) for the
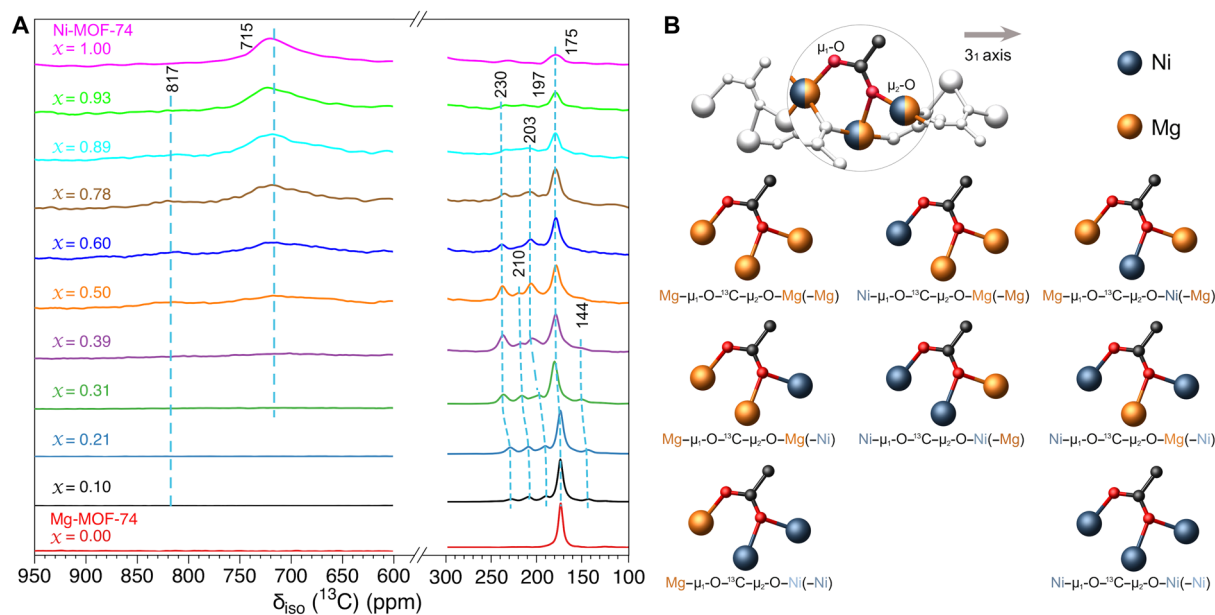
Fig. 3. NMR spectra and local bonding configurations for Mg$_{1-x}$Ni$_x$-MOF-74. (**A**) ^{13}C MAS NMR spectra of methanol-exchanged Mg$_{1-x}$Ni$_x$-MOF-74 within selected regions (the full spectra are shown in fig. S13). The weak peak at 175 ppm in the spectrum of Ni-MOF-74 is due to defects such as dangling carboxylates at the terminal crystallite surface. These carboxylates are not affected by Ni^{2+} but exhibit similar ^{13}C chemical shift as that of Mg-MOF-74. (**B**) Eight possible Ni/Mg arrangements labeled with a ^{13}C-carboxylate.

three metal ions labeled with a ^{13}C-carboxylate, namely, Mg—μ$_1$-O—^{13}C—μ$_2$-O—Mg(−Mg), Ni—μ$_1$-O—^{13}C—μ$_2$-O—Mg(−Mg), Mg—μ$_1$-O—^{13}C—μ$_2$-O—Ni(−Mg), Mg—μ$_1$-O—^{13}C—μ$_2$-O—Mg(−Ni), Ni—μ$_1$-O—^{13}C—μ$_2$-O—Ni(−Mg), Ni—μ$_1$-O—^{13}C—μ$_2$-O—Mg(−Ni), Mg—μ$_1$-O—^{13}C—μ$_2$-O—Ni(−Ni), and Ni—μ$_1$-O—^{13}C—μ$_2$-O—Ni(−Ni).

We thus postulate that five narrow and three broad peaks shown in SSNMR results are corresponding to the eight modes of Mg/Ni arrangements. The distinct ^{13}C NMR chemical shifts and linewidths are expected to originate from different magnetic coupling schemes, i.e., the type of interaction between unpaired electrons of paramagnetic Ni^{2+} ions and adjacent or even remote unpaired electrons of other Ni^{2+} ions. Both FM (i.e., electronic spins are parallelly aligned) coupling and AFM (i.e., electronic spins are antiparallelly aligned) coupling of Ni^{2+} are witnessed in (pure nickel) Ni-MOF-74, whereas the FM coupling is stronger (*23*). We suspect that the Ni^{2+} ions in Mg$_{1-x}$Ni$_x$-MOF-74 samples interact with each other in a similar manner on the basis of magnetic susceptibility measurements (figs. S26 to S31). As a result, the Mg/Ni arrangement in which Ni^{2+} ions are FM-coupled induces broad ^{13}C NMR peaks, characteristic of paramagnetic solids, and the Mg/Ni arrangement in which Ni^{2+} ions are AFM-coupled generates much narrower ^{13}C NMR peaks with similar spectral features to those found in diamagnetic Mg-MOF-74 (*6*, *16*, *17*).

We first assigned the broad peak at 715 ppm and the narrow peak at 175 ppm to the carbon in Ni—μ$_1$-O—^{13}C—μ$_2$-O—Ni(−Ni) and Mg—μ$_1$-O—^{13}C—μ$_2$-O—Mg(−Mg), respectively, based on the observed NMR spectra of monometallic MOF-74 samples. We then used the two magnetic coupling schemes to assign the remaining six peaks. The two broad peaks at 817 and 197 ppm correspond to Ni—μ$_1$-O—^{13}C—μ$_2$-O—Ni(−Mg) and Mg—μ$_1$-O—^{13}C—μ$_2$-O—Ni(−Ni) arrangements due to the FM coupling between two adjacent Ni^{2+} ions, whereas the four narrow peaks at 230, 210, 203, and 144 ppm

are attributed to Ni—μ$_1$-O—^{13}C—μ$_2$-O—Mg(−Ni), Ni—μ$_1$-O—^{13}C—μ$_2$-O—Mg(−Mg), Mg—μ$_1$-O—^{13}C—μ$_2$-O—Ni(−Mg), and Mg—μ$_1$-O—^{13}C—μ$_2$-O—Mg(−Ni) arrangements, with AFM-coupled Ni^{2+} ions.

Assignment of ^{13}C peaks within each magnetic coupling scheme can be empirically accomplished by examining the role that unpaired electrons play in contributing to the ^{13}C chemical shifts. Here, we follow the precedent wherein chemical shift changes are additive through bonds and are sensitive to the distance between the paramagnetic ion and the observed NMR nucleus (*13*). Figure 4A illustrates the spatial distribution of metal ions relative to carboxylate groups, from which we analyzed the distances and bond angles between Ni^{2+} ion at different positions (M2 to M4) and the ^{13}C nucleus of carboxylate (C4). The distances are found to be M2—C4 < M4—C4 < M3—C4, and the metal-oxygen-carbon angles are also ordered as M2—O—C4 < M4—O—C4 < M3—O—C4. Considering that the effect of unpaired electrons at the carboxylate carbon decreases with increasing through-bond distance, we estimate the magnitude of chemical shift change induced by paramagnetic Ni^{2+} ions (i.e., |chemical shift of paramagnetic substance − chemical shift of diamagnetic analog|) and then assign the NMR peaks accordingly. For the FM-coupled scheme of ^{13}C chemical shifts, the arrangement with two adjacent Ni^{2+} ions at M2 and M3 positions results in greater chemical shift changes [Ni—μ$_1$-O—^{13}C—μ$_2$-O—Ni(−Mg): |817 ppm − 175 ppm|] than that with Ni^{2+} ions at M3 and M4 positions [Mg—μ$_1$-O—^{13}C—μ$_2$-O—Ni(−Ni): |197 ppm − 175 ppm|]. Turning to the four narrow ^{13}C peaks within the AF-coupled scheme, they may also be assigned according to the distance of the ^{13}C nuclei from unpaired electrons in the following order: Ni—μ$_1$-O—^{13}C—μ$_2$-O—Mg(−Ni) (|230 ppm − 175 ppm|) > Ni—μ$_1$-O—^{13}C—μ$_2$-O—Mg(−Mg) (|210 ppm − 175 ppm|) > Mg—μ$_1$-O—^{13}C—μ$_2$-O—Mg(−Ni) (|144 ppm − 175 ppm|) > Mg—μ$_1$-O—^{13}C—μ$_2$-O—Ni(−Mg) (|203 ppm − 175 ppm|). We also notice that the differences between observed chemical shifts of paramagnetic
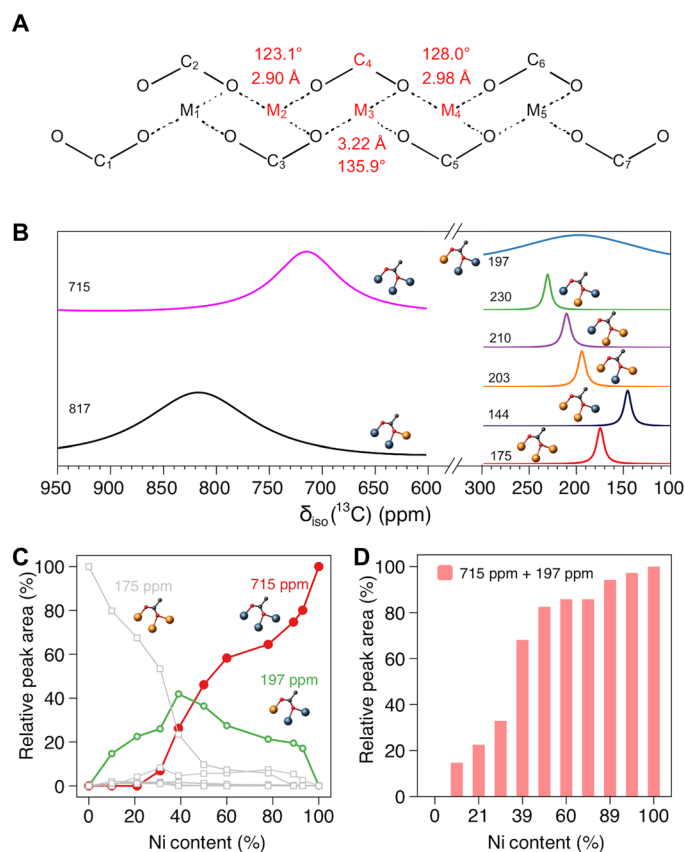
A

B

C **D**

Fig. 4. Speciation and quantification of local bonding environments in $Mg_{1-x}Ni_x$-MOF-74. (**A**) Schematic illustration of the connectivity between carboxylate groups and metal ions in $Mg_{1-x}Ni_x$-MOF-74. The carboxylate and metal ions of interest and corresponding M—C distances and M—O—C angles are highlighted in red. (**B**) Assignment of ^{13}C NMR peaks to corresponding atomic-scale Ni/Mg arrangements. (**C**) Abundance of each ^{13}C NMR peak as a function of the Ni content. The three peaks at 175, 197, and 715 ppm are labeled for clarity. The abundance of other peaks is always less than 10% for all compositions. The estimated error is ±0.2%. (**D**) Abundance of two peaks at 197 and 715 ppm as a function of the Ni content.

substance and diamagnetic analog are largest when the M—O—C bond angle approaches 109.5°, affirming that the magnitude of these through-bond effects are sensitive to delocalization of unpaired electron spin density through M—O—C bonds (*13*).

A more compelling assignment of the observed ^{13}C NMR peaks requires ab initio DFT calculations, which are believed to be reliable in predicting the relative peak positions for sequential NMR signals (*24–26*). Here, we used the NorthWest computational Chemistry (NWChem, version 6.5) software package to perform DFT calculations (*27, 28*). Calculations of chemical shifts in the presence of paramagnetic centers via DFT are fraught with difficulties, yet the order of calculated chemical shifts as a function of distance from the paramagnetic center is expected to follow the order of observed peak shifts, although the magnitude of calculated numbers may be quite different from observed shifts (*6, 12–15, 29, 30*). Specifically, we used a cluster model consisting of five metal ions (fig. S32) and calculated the chemical shift of the carboxylate carbon in specific Mg/Ni arrangement (tables S3 to S5 and fig. S33). Two additional magnesium ions and corresponding organic linkers were included in this model cluster to improve the accuracy of predicted chemical shift.

The two broad peaks at 817 and 197 ppm and the four narrow peaks at 230, 210, 203, and 144 ppm have to be assigned separately because of their distinct magnetic coupling schemes. According to our DFT analyses, the chemical shifts are predicted to be 4333 ppm for Ni—μ_1-O—^{13}C—μ_2-O—Ni(—Mg) and 766 ppm for Mg—μ_1-O—^{13}C—μ_2-O—Ni(—Ni), respectively. Using the order of calculated chemical shift as a guide, we assigned the peak at 817 ppm to Ni—μ_1-O—^{13}C—μ_2-O—Ni(—Mg) and the peak at 197 ppm to Mg—μ_1-O—^{13}C—μ_2-O—Ni(—Ni). Similarly, the order of calculated chemical shifts is 252 ppm [Ni—μ_1-O—^{13}C—μ_2-O—Mg(—Ni)] > 204 ppm [Ni—μ_1-O—^{13}C—μ_2-O—Mg(—Mg)] > 190 ppm [Mg—μ_1-O—^{13}C—μ_2-O—Ni(—Mg)] > 184 ppm [Mg—μ_1-O—^{13}C—μ_2-O—Mg(—Ni)] for the other Mg/Ni arrangements, and the four narrow peaks at 230, 210, 203, and 144 ppm were assigned accordingly. Assignment from the computational approach is consistent with that from the empirical approach (table S6), and the results are shown in Fig. 4B.

We then calculated the abundance of each Mg/Ni arrangement in $Mg_{1-x}Ni_x$-MOF-74 samples (Fig. 4C), considering that the NMR peak area is proportional to the number of ^{13}C nuclei in corresponding chemical environment (figs. S34 to S35). After Ni incorporation, the compositional contribution of Mg—μ_1-O—^{13}C—μ_2-O—Mg(—Mg) gradually decreases from 100 to 0%, as expected. The Mg—μ_1-O—^{13}C—μ_2-O—Ni(—Ni) and Ni—μ_1-O—^{13}C—μ_2-O—Ni(—Ni) arrangements, featuring the "Ni—μ_2-O—Ni" bonding mode, are unexpectedly predominant in atomic-scale metal heterogeneity in nearly all MOF samples (Fig. 4D). The two arrangements together constitute more than 80% of all eight arrangements when $x > 0.39$ and more than 70% of seven Ni-containing arrangements even in the sample of $x = 0.10$ (fig. S36). Specifically, the Mg—μ_1-O—^{13}C—μ_2-O—Ni(—Ni) arrangement dominates in the region of $x = 0.10$ to 0.39, whereas the Ni—μ_1-O—^{13}C—μ_2-O—Ni(—Ni) arrangement dominates in the region of $x = 0.50$ to 0.93. This important observation is contrary to the common notion that solution mixing of starting materials in one-pot synthesis will yield random metal apportionment in mixed-metal MOFs. The dominance of two Mg/Ni arrangements among all eight arrangements is attributed to the marked effect of FM coupling in stabilizing the Ni—μ_2-O—Ni–type environments (fig. S37).

Macroscopic adsorption phenomena

The SSNMR analysis here provides a unique yet reliable approach to create a direct correlation between the controllable macroscopic-scale material preparation and the previously inaccessible atomic-scale metal apportionment. We anticipate that this correlation may be further extended to the macroscopic properties of mixed-metal MOFs. Toward this end, we explored the relationship between metal apportionment and macroscopic properties by monitoring gas adsorption, as it is one of the most important applications of MOFs (*31*). Carbon monoxide (CO) was chosen as a representative example because it is highly valuable and its use is essential in the production of many chemicals (*32*). It has been demonstrated that the adsorption behavior of CO/CO_2 on activated Ni-MOF-74 is distinct from activated Mg-MOF-74 (*33, 34*): CO adsorption is preferential on Ni-MOF-74 via the formation of strong Ni—C bonds, whereas the pore surface of Mg-MOF-74 is primarily covered by CO_2 through weak physical adsorption. We thus postulate that fine-tuning of atomic-scale metal apportionments in $Mg_{1-x}Ni_x$-MOF-74 samples, mainly the compositional change in Mg—μ_1-O—^{13}C—μ_2-O—Ni(—Ni) and Ni—μ_1-O—^{13}C—μ_2-O—Ni(—Ni) arrangements, may yield different CO adsorption behavior compared to their monometallic

counterparts. In addition, this strategy may allow for effective separation of CO from gas stream containing certain amounts of CO_2, making a more facile CO recovery process.

We test this postulation by first performing DFT calculations to elucidate the adsorption behavior of CO on model clusters representing $Mg—\mu_1\text{-}O—^{13}C—\mu_2\text{-}O—Ni(—Ni)$ and $Ni—\mu_1\text{-}O—^{13}C—\mu_2\text{-}O—Ni(—Ni)$ arrangements, respectively (Fig. 5A). According to our computational results, CO molecule prefers to adopt strong chemical adsorption on Ni^{2+} via "terminal binding" in both arrangements, whereas the physical adsorption of CO on Mg^{2+} is remarkably weaker (33–36). The $Mg—\mu_1\text{-}O—^{13}C—\mu_2\text{-}O—Ni(—Ni)$ arrangement, however, allows for "bridge binding" of the second CO molecule on each Ni^{2+}. This binding mode is thermodynamically stable, as reflected by a mean CO adsorption energy of −44 kJ/mol. It is worth mentioning that the Ni^{2+} and Mg^{2+} ions involved in the bridge binding mode are related by the 3_1 axis and thus are exposed to the same MOF

channel (fig. S38). In contrast, further DFT explorations suggest that the incorporation of bridge binding CO molecules is perturbed by two adjacent terminal binding CO molecules in Ni-MOF-74 (fig. S39).

We conducted breakthrough experiments to gain insights into CO/CO_2 adsorption as a consequence of tuning atomic-scale metal apportionment. Before these adsorption measurements, the MOFs were activated to evacuate methanol and yield open metal sites (9). We monitored the concentrations of eluents immediately after the gas stream passed through a column packed with activated MOFs as a function of retention time (Fig. 5B and fig. S40). The CO_2 uptake by Mg-MOF-74 ($x = 0.00$) is preferential, as reflected by a long breakthrough time of 8.20 min, whereas observation of a very short breakthrough time of 0.75 min is indicative of ineffective CO adsorption on Mg^{2+} (table S7) (34). Nevertheless, the breakthrough time of CO becomes noticeably longer when Ni is incorporated and surpasses that of CO_2 when the Ni content is beyond 21%. All recorded CO
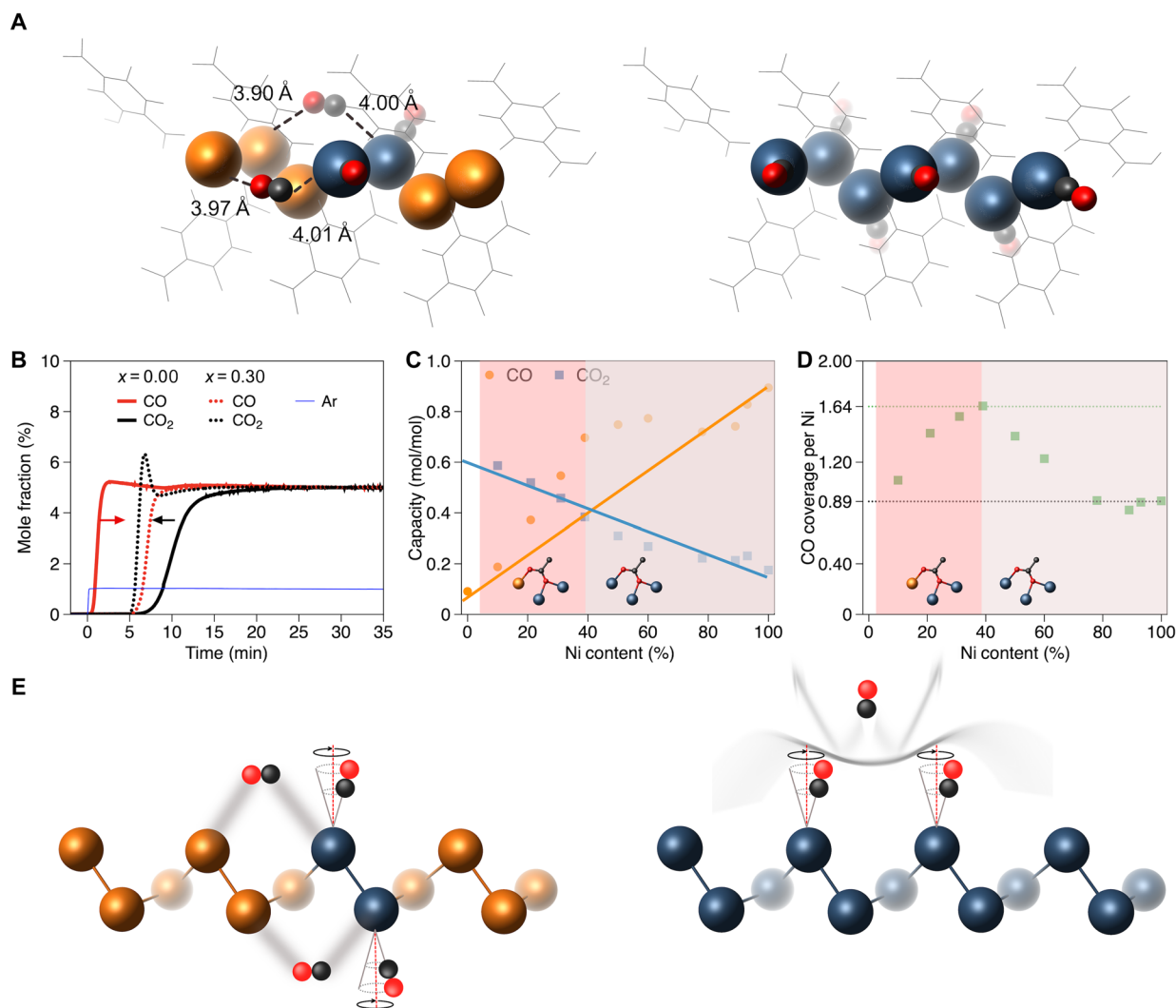

Fig. 5. CO/CO2 gas mixtures adsorbed onto Mg1−xNix-MOF-74. (**A**) The adsorption configurations of CO on model clusters representing $Mg—\mu_1\text{-}O—^{13}C—\mu_2\text{-}O—Ni(—Ni)$ (left) and $Ni—\mu_1\text{-}O—^{13}C—\mu_2\text{-}O—Ni(—Ni)$ (right) arrangements, respectively. (**B**) Selected breakthrough curves of CO/CO_2 in a $CO/CO_2/Ar/He$ flow (5:5:1:89 volume %) for activated Mg1−xNix-MOF-74 samples. The Ar and He were introduced as internal reference and carrier gas, respectively. (**C**) CO/CO2 adsorption capacity as a function of the Ni content. (**D**) CO coverage per Ni as a function of the Ni content. (**E**) Schematic illustration of the mechanism of higher CO coverage per Ni allowed for Mg0.61Ni0.39-MOF-74 than Ni-MOF-74.

breakthrough curves of $Mg_{1-x}Ni_x$-MOF-74 samples ($x > 0.21$) exhibit a roll-up feature, which resembles the characteristics found in CO/CO_2 breakthrough experiment of Ni-MOF-74 (33, 34). These results strongly support our hypothesis that the predominant atomic-scale $Mg-\mu_1-O-^{13}C-\mu_2-O-Ni(-Ni)$ and $Ni-\mu_1-O-^{13}C-\mu_2-O-Ni(-Ni)$ arrangements in these MOF samples (Fig. 4D) are crucial in determination of the macroscopic CO adsorption performance.

We then calculated the adsorption capacity of CO/CO_2 as a function of the macroscopic material composition (fig. S41 and table S7) to better interpret breakthrough data. As shown in Fig. 5C, CO_2 adsorption on $Mg_{1-x}Ni_x$-MOF-74 is not governed by any particular atomic-scale metal apportionment but, alternatively, by the averaged macroscopic composition, as evidenced by the linearly decreasing CO_2 adsorption capacity with increasing Ni content. This observation is consistent with the notion that incorporation of more Ni into the MOFs results in less available Mg^{2+} sites for CO_2 adsorption. Unlike the case of CO_2, CO adsorption capacity of measured MOF sample notably and nonlinearly grows with increasing Ni content. These CO capacity results can be interpreted by splitting the full compositional scale into two regions of the atomic-scale $Mg-\mu_1-O-^{13}C-\mu_2-O-Ni(-Ni)$ and $Ni-\mu_1-O-^{13}C-\mu_2-O-Ni(-Ni)$ arrangements: For the region of $x < 0.4$, the emergence of $Mg-\mu_1-O-^{13}C-\mu_2-O-Ni(-Ni)$ enables drastically improved CO adsorption; for the region of $x > 0.4$, $Ni-\mu_1-O-^{13}C-\mu_2-O-Ni(-Ni)$ becomes the major (or predominant) in all atomic-scale arrangements and CO adsorption capacity of corresponding $Mg_{1-x}Ni_x$-MOF-74 gradually resembles that of monometallic Ni-MOF-74. Hence, only a slight difference in CO capacity is observed with the Ni content ranging from 0.4 to 1.0. We converted CO adsorption capacity to CO coverage per Ni (Fig. 5D) and observed that the coverage ramps up from 1.06 ($x = 0.10$) to its maxima of 1.64 ($x = 0.39$) and then steadily declines to the value comparable to that of Ni-MOF-74 (0.89; $x = 1.00$) (35, 36). This decline results from the steric hindrance from two terminal binding CO molecules on adjacent Ni^{2+} ions within the same channel, and the perturbance is further amplified by the wobbling of CO molecules about the time-averaged position at ambient temperature (Fig. 5E) (36, 37).

DISCUSSION

We have uncovered nonrandom atomic-scale metal apportionment in mixed-metal MOFs by SSNMR and further establish the relationship between metal apportionment and macroscopic observables by breakthrough experiments. Moreover, we exploit apportionment assessment to propose a new functional material ($Mg_{0.61}Ni_{0.39}$-MOF-74) for potential industrial application of CO adsorption. This specific metal composition and apportionment result in a higher atom economy of Ni than Ni-MOF-74, requiring only half of Ni^{2+} for the same amount of adsorbed CO gases. Note that the substitution of Ni with earth-abundant and nontoxic Mg in $Mg_{0.61}Ni_{0.39}$-MOF-74 also improves the humidity tolerance of MOFs during gas adsorption (38, 39) and yields enhanced catalytic activity and stability in reactions such as (de)hydrogenation of alcohols (40). The SSNMR-accessible atomic-scale metal apportionment thus fills the gap between rational design of macroscopic scale material preparation and creation of superior macroscopic scale performance of mixed-metal MOFs. We envision that this nondestructive SSNMR methodology can be further applied to analyze bulk assembly of other mixed-metal MOFs such as $Mg_{1-x}Co_x$-MOF-74. The preliminary results shed light

on the unique magnetic properties of these samples, and we will report the thorough work in the future.

MATERIALS AND METHODS
Sample preparation
Hydroquinone ($\geq99\%$), potassium carbonate-^{13}C (98 at % ^{13}C), potassium formate (99%), sodium sulfite ($\geq98\%$), 2,5-dihydroxy-terephthalic acid (H_4DHTP; 98%), magnesium nitrate hexahydrate (99.999% trace metal basis), nickel(II) nitrate hexahydrate (99.999% trace metal basis), hydrochloric acid (37%; ACS reagent), and ethanol ($\geq 99.5\%$) were purchased from Sigma-Aldrich. Anhydrous N,N'-dimethylformamide (DMF) and methanol were obtained from EMD Millipore Chemicals. Ultrahigh-purity grade CO gas (99.999% purity) was obtained from Praxair. All starting materials and solvents, unless otherwise specified, were used without further purification.

The synthesis of $^{13}COOH$-labeled H_4DHTP ($H_4DHTP-^{13}C_2$) is modified from the published procedure (41). A glass branched seal tube was filled with a mixture of hydroquinone (0.714 g, 6.48 mmol), ^{13}C-labeled potassium carbonate (1.00 g, 7.18 mmol), and potassium formate (1.60 g) and flushed for three cycles (vacuum/CO_2). The reaction mixture was then heated to 200°C under CO_2 atmosphere for 4 hours. The yellow product was slowly cooled down to room temperature before adding to 30 ml of 0.5 weight % sodium sulfite aqueous solution. The yellow product was precipitated with hydrochloric acid (37%), washed with water (10 ml × 3), filtered off, and dried under vacuum at 50°C to give $H_4DHTP-^{13}C_2$ a bright solid yellow color (yield: 0.653 g, 3.26 mmol, 50%).

Methanol-exchanged $Mg_{1-x}Ni_x$-MOF-74 samples were synthesized following the published procedure (8). Typically, H_4DHTP or $H_4DHTP-^{13}C_2$ (40.0 mg, 0.200 mmol) and a stoichiometric (table S1) mixture of $Mg(NO_3)_2\cdot6H_2O$ and $Ni(NO_3)_2\cdot6H_2O$ (0.617 mmol in total) were dissolved in $DMF/ethanol/H_2O$ (15 ml/1 ml/1 ml) and placed in a 20-ml scintillation vial, which was heated to 120°C for 20 hours. The precipitate was collected, washed, and immersed in 20 ml of anhydrous DMF for 3 days, during which time the DMF was refreshed three times per day. The DMF-exchanged compound was filtrated off and immersed in 20 ml of anhydrous methanol for 3 days, during which time the methanol was also refreshed three times per day. Natural abundance samples were used in ICP-OES, scanning electron microscopy, EDX, magnetic susceptibility, and breakthrough measurements, while $^{13}COO^-$-labeled samples were used in SSNMR measurements.

Characterizations
The details of PXRD, ICP-OES, scanning electron microscopy, EDS, SSNMR, magnetic susceptibility, CO/CO_2 breakthrough measurements, and DFT calculations are provided in the Supplementary Materials.

REFERENCES AND NOTES
1. O. M. Yaghi, M. J. Kalmutzki, C. S. Diercks, *Introduction to Reticular Chemistry: Metal-Organic Frameworks and Covalent Organic Frameworks* (Wiley-VCH, 2019), pp. 552.
2. S. Abednatanzi, P. Gohari Derakhshandeh, H. Depauw, F.-X. Coudert, H. Vrielinck, P. van der Voort, K. Leus, Mixed-metal metal–organic frameworks. *Chem. Soc. Rev.* **48**, 2535–2565 (2019).

3. M. Y. Masoomi, A. Morsali, A. Dhakshinamoorthy, H. Garcia, Mixed-metal MOFs: Unique opportunities in metal–organic framework (MOF) functionality and design. *Angew. Chem. Int. Ed.* **58**, 15188–15205 (2019).

4. X. Kong, H. Deng, F. Yan, J. Kim, J. A. Swisher, B. Smit, O. M. Yaghi, J. A. Reimer, Mapping of functional groups in metal-organic frameworks. *Science* **341**, 882–885 (2013).

5. M. Baias, A. Lesage, S. Aguado, J. Canivet, V. Moizan-Basle, N. Audebrand, D. Farrusseng, L. Emsley, Superstructure of a substituted zeolitic imidazolate metal–organic framework determined by combining proton solid-state NMR spectroscopy and DFT calculations. *Angew. Chem. Int. Ed.* **54**, 5971–5976 (2015).

6. G. Mali, M. Mazaj, I. Arčon, D. Hanžel, D. Arčon, Z. Jagličić, Unraveling the arrangement of Al and Fe within the framework explains the magnetism of mixed-metal MIL-100(Al,Fe). *J. Phys. Chem. Lett.* **10**, 1464–1470 (2019).

7. Z. Ji, T. Li, O. M. Yaghi, Sequencing of metals in multivariate metal-organic frameworks. *Science* **369**, 674–680 (2020).

8. L. J. Wang, H. Deng, H. Furukawa, F. Gándara, K. E. Cordova, D. Peri, O. M. Yaghi, Synthesis and characterization of metal–organic framework-74 containing 2, 4, 6, 8, and 10 different metals. *Inorg. Chem.* **53**, 5881–5883 (2014).

9. P. D. C. Dietzel, R. Blom, H. Fjellvåg, Base-induced formation of two magnesium metal-organic framework compounds with a bifunctional tetratopic ligand. *Eur. J. Inorg. Chem.* **2008**, 3624–3632 (2008).

10. A. J. Pell, G. Pintacuda, C. P. Grey, Paramagnetic NMR in solution and the solid state. *Prog. Nucl. Magn. Reson. Spectrosc.* **111**, 1–271 (2019).

11. N. D. Jensen, C. Forano, S. S. C. Pushparaj, Y. Nishiyama, B. Bekele, U. G. Nielsen, The distribution of reactive Ni^{2+} in 2D $Mg_{2−x}Ni_xAl$-LDH nanohybrid materials determined by solid state ^{27}Al MAS NMR spectroscopy. *Phys. Chem. Chem. Phys.* **20**, 25335–25342 (2018).

12. I. D. Seymour, D. S. Middlemiss, D. M. Halat, N. M. Trease, A. J. Pell, C. P. Grey, Characterizing oxygen local environments in paramagnetic battery materials via ^{17}O NMR and DFT calculations. *J. Am. Chem. Soc.* **138**, 9405–9408 (2016).

13. R. J. Clément, A. J. Pell, D. S. Middlemiss, F. C. Strobridge, J. K. Miller, M. S. Whittingham, L. Emsley, C. P. Grey, G. Pintacuda, Spin-transfer pathways in paramagnetic lithium transition-metal phosphates from combined broadband isotropic solid-state MAS NMR spectroscopy and DFT calculations. *J. Am. Chem. Soc.* **134**, 17178–17185 (2012).

14. T. Wittmann, A. Mondal, C. B. L. Tschense, J. J. Wittmann, O. Klimm, R. Siegel, B. Corzilius, B. Weber, M. Kaupp, J. Senker, Probing interactions of N-donor molecules with open metal sites within paramagnetic Cr-MIL-101: A solid-state NMR spectroscopic and density functional theory study. *J. Am. Chem. Soc.* **140**, 2135–2144 (2018).

15. X. Kong, V. V. Terskikh, R. L. Khade, L. Yang, A. Rorick, Y. Zhang, P. He, Y. Huang, G. Wu, Solid-state ^{17}O NMR spectroscopy of paramagnetic coordination compounds. *Angew. Chem. Int. Ed.* **54**, 4753–4757 (2015).

16. M. Rauche, S. Ehrling, S. Krause, I. Senkovska, S. Kaskel, E. Brunner, New insights into solvent-induced structural changes of ^{13}C labelled metal–organic frameworks by solid state NMR. *Chem. Commun.* **55**, 9140–9143 (2019).

17. J. Blahut, A. L. Lejeune, S. Ehrling, I. Senkovska, S. Kaskel, F. M. Wisser, G. Pintacuda, Monitoring dynamics, structure, and magnetism of switchable metal–organic frameworks via ^1H-detected MAS NMR. *Angew. Chem. Int. Ed.* **60**, 21778–21783 (2021).

18. D. I. Kolokolov, H. Jobic, A. G. Stepanov, V. Guillerm, T. Devic, C. Serre, G. Férey, Dynamics of benzene rings in MIL-53(Cr) and MIL-47(V) frameworks studied by ^2H NMR spectroscopy. *Angew. Chem. Int. Ed.* **49**, 4791–4794 (2010).

19. D. M. Dawson, L. E. Jamieson, M. I. H. Mohideen, A. C. McKinlay, I. A. Smellie, R. Cadou, N. S. Keddie, R. E. Morris, S. E. Ashbrook, High-resolution solid-state ^{13}C NMR spectroscopy of the paramagnetic metal–organic frameworks, STAM-1 and HKUST-1. *Phys. Chem. Chem. Phys.* **15**, 919–929 (2013).

20. R. Giovine, F. Pourpoint, S. Duval, O. Lafon, J. P. Amoureux, T. Loiseau, C. Volkringer, The surprising stability of $Cu_3(btc)_2$ metal–organic framework under steam flow at high temperature. *Cryst. Growth Des.* **18**, 6681–6693 (2018).

21. C. Li, X. Hu, X. Lou, L. Zhang, Y. Wang, J. P. Amoureux, M. Shen, Q. Chen, B. Hu, The organic-moiety-dominated Li^+ intercalation/deintercalation mechanism of a cobalt-based metal–organic framework. *J. Mater. Chem. A* **4**, 16245–16251 (2016).

22. J. Xu, V. V. Terskikh, Y. Huang, ^{25}Mg solid-state NMR: A sensitive probe of adsorbing guest molecules on a metal center in metal–organic framework CPO-27-Mg. *J. Phys. Chem. Lett.* **4**, 7–11 (2013).

23. S. Muratović, B. Karadeniz, T. Stolar, S. Lukin, I. Halasz, M. Herak, G. Mali, Y. Krupskaya, V. Kataev, D. Žilić, K. Užarević, Impact of dehydration and mechanical amorphization on the magnetic properties of Ni(ii)-MOF-74. *J. Mater. Chem. C* **8**, 7132–7142 (2020).

24. E. Salager, G. M. Day, R. S. Stein, C. J. Pickard, B. Elena, L. Emsley, Powder crystallography by combined crystal structure prediction and high-resolution ^1H solid-state NMR spectroscopy. *J. Am. Chem. Soc.* **132**, 2564–2566 (2010).

25. D. Laurencin, C. Gervais, A. Wong, C. Coelho, F. Mauri, D. Massiot, M. E. Smith, C. Bonhomme, Implementation of high resolution ^{43}Ca solid state NMR spectroscopy: Toward the elucidation of calcium sites in biological materials. *J. Am. Chem. Soc.* **131**, 13430–13440 (2009).

26. V. Martins, J. Xu, X. Wang, K. Chen, I. Hung, Z. Gan, C. Gervais, C. Bonhomme, S. Jiang, A. Zheng, B. E. G. Lucier, Y. Huang, Higher magnetic fields, finer MOF structural information: ^{17}O solid-state NMR at 35.2 T. *J. Am. Chem. Soc.* **142**, 14877–14889 (2020).

27. M. Valiev, E. J. Bylaska, N. Govind, K. Kowalski, T. P. Straatsma, H. J. J. van Dam, D. Wang, J. Nieplocha, E. Apra, T. L. Windus, W. A. de Jong, NWChem: A comprehensive and scalable open-source solution for large scale molecular simulations. *Comput. Phys. Commun.* **181**, 1477–1489 (2010).

28. F. Aquino, B. Pritchard, J. Autschbach, Scalar relativistic computations and localized orbital analyses of nuclear hyperfine coupling and paramagnetic NMR chemical shifts. *J. Chem. Theory Comput.* **8**, 598–609 (2012).

29. G. Kervern, G. Pintacuda, Y. Zhang, E. Oldfield, C. Roukoss, E. Kuntz, E. Herdtweck, J. M. Basset, S. Cadars, A. Lesage, C. Copéret, L. Emsley, Solid-State NMR of a paramagnetic DIAD-FeII catalyst: Sensitivity, resolution enhancement, and structure-based assignments. *J. Am. Chem. Soc.* **128**, 13545–13552 (2006).

30. Z. Ke, D. M. Dawson, S. E. Ashbrook, M. Bühl, Origin of the temperature dependence of ^{13}C pNMR shifts for copper paddlewheel MOFs. *Chem. Sci.* **13**, 2674–2685 (2022).

31. H. Furukawa, K. E. Cordova, M. O'Keeffe, O. M. Yaghi, The chemistry and applications of metal-organic frameworks. *Science* **341**, 1230444 (2013).

32. J. Bierhals, Carbon monoxide, in *Ullmann's Encyclopedia of Industrial Chemistry* (Wiley-VCH, 2001).

33. E. J. García, J. P. S. Mowat, P. A. Wright, J. Pérez-Pellitero, C. Jallut, G. D. Pirngruber, Role of structure and chemistry in controlling separations of CO_2/CH_4 and $CO_2/CH_4/CO$ mixtures over honeycomb MOFs with coordinatively unsaturated metal sites. *J. Phys. Chem. C* **116**, 26636–26648 (2012).

34. H. Kim, M. Sohail, K. Yim, Y. C. Park, D. H. Chun, H. J. Kim, S. O. Han, J. H. Moon, Effective CO_2 and CO separation using $[M_2(DOBDC)]$ (M = Mg, Co, Ni) with unsaturated metal sites and excavation of their adsorption sites. *ACS Appl. Mater. Interfaces* **11**, 7014–7021 (2019).

35. S. Chavan, J. G. Vitillo, E. Groppo, F. Bonino, C. Lamberti, P. D. C. Dietzel, S. Bordiga, CO adsorption on CPO-27-Ni coordination polymer: Spectroscopic features and interaction energy. *J. Phys. Chem. C* **113**, 3292–3299 (2009).

36. E. D. Bloch, M. R. Hudson, J. A. Mason, S. Chavan, V. Crocellà, J. D. Howe, K. Lee, A. L. Dzubak, W. L. Queen, J. M. Zadrozny, S. J. Geier, L. C. Lin, L. Gagliardi, B. Smit, J. B. Neaton, S. Bordiga, C. M. Brown, J. R. Long, Reversible CO binding enables tunable CO/H_2 and CO/N_2 separations in metal–organic frameworks with exposed divalent metal cations. *J. Am. Chem. Soc.* **136**, 10752–10761 (2014).

37. B. E. G. Lucier, H. Chan, Y. Zhang, Y. Huang, Multiple modes of motion: Realizing the dynamics of CO adsorbed in M-MOF-74 (M = Mg, Zn) by using solid-state NMR spectroscopy. *Eur. J. Inorg. Chem.* **2016**, 2017–2024 (2016).

38. Y. Jiao, C. R. Morelock, N. C. Burtch, W. P. Mounfield III, J. T. Hungerford, K. S. Walton, Tuning the kinetic water stability and adsorption interactions of Mg-MOF-74 by partial substitution with Co or Ni. *Ind. Eng. Chem. Res.* **54**, 12408–12414 (2015).

39. J. D. Howe, C. R. Morelock, Y. Jiao, K. W. Chapman, K. S. Walton, D. S. Sholl, Understanding structure, metal distribution, and water adsorption in mixed-metal MOF-74. *J. Phys. Chem. C* **121**, 627–635 (2017).

40. J. L. Snider, J. Su, P. Verma, F. el Gabaly, J. D. Sugar, L. Chen, J. M. Chames, A. A. Talin, C. Dun, J. J. Urban, V. Stavila, D. Prendergast, G. A. Somorjai, M. D. Allendorf, Stabilized open metal sites in bimetallic metal–organic framework catalysts for hydrogen production from alcohols. *J. Mater. Chem. A* **9**, 10869–10881 (2021).

41. D. J. Sikkema, A. M. Reichwein, Process for dicarboxylating dihydric phenols. U.S. Patent 6,40,478, (2000).

42. B. H. Toby, R. B. Von Dreele, GSAS-II: The genesis of a modern open-source all purpose crystallography software package. *J. Appl. Cryst.* **46**, 544–549 (2013).

43. S. W. Sparks, P. D. Ellis, Platinum-195 shielding tensors in potassium hexachloroplatinate(IV) and potassium tetrachloroplatinate(II). *J. Am. Chem. Soc.* **108**, 3215–3218 (1986).

44. D. Massiot, F. Fayon, M. Capron, I. King, S. le Calvé, B. Alonso, J. O. Durand, B. Bujoli, Z. Gan, G. Hoatson, Modelling one- and two-dimensional solid-state NMR spectra. *Magn. Reson. Chem.* **40**, 70–76 (2002).

45. M. D. Walter, M. Schultz, R. A. Andersen, Weak paramagnetism in compounds of the type $Cp'_2Yb(bipy)$. *New J. Chem.* **30**, 238–246 (2006).

46. R. L. Halbach, G. Nocton, C. H. Booth, L. Maron, R. A. Andersen, Cerium tetrakis(tropolonate) and cerium tetrakis(acetylacetonate) are not diamagnetic but temperature-independent paramagnets. *Inorg. Chem.* **57**, 7290–7298 (2018).

47. G. A. Bain, J. F. Berry, Diamagnetic corrections and Pascal's constants. *J. Chem. Educ.* **85**, 532 (2008).

48. A. Nayeem, J. P. Yesinowski, Calculation of magic-angle spinning nuclear magnetic resonance spectra of paramagnetic solids. *J. Chem. Phys.* **89**, 4600–4608 (1988).

49. K. S. Min, A. L. Rhinegold, J. S. Miller, Synthesis, structure, and magnetic ordering of layered (2-D) V-based tris(oxalato)metalates. *Inorg. Chem.* **44**, 8433–8441 (2005).

50. C. A. L. Filgueiras, A. Horn Jr., R. A. Howie, J. M. S. Skakle, J. L. Wardell, α-Form of tris(2,4-pentanedionato-O,O')vanadium(III), re-refinement against new intensity data. *Acta Crystallogr. E* **57**, m157–m158 (2001).

51. D. Feller, The role of databases in support of computational chemistry calculations. *J. Comput. Chem.* **17**, 1571–1586 (1996).

52. K. L. Schuchardt, B. T. Didier, T. Elsethagen, L. Sun, V. Gurumoorthi, J. Chase, J. Li, T. L. Windus, Basis set exchange: A community database for computational sciences. *J. Chem. Inf. Model.* **47**, 1045–1052 (2007).

53. R. E. Wasylishen, D. L. Bryce, A revised experimental absolute magnetic shielding scale for oxygen. *J. Chem. Phys.* **117**, 10061–10066 (2002).

54. M. J. Frisch, G. W. Trucks, H. B. Schlegel, G. E. Scuseria, M. A. Robb, J. R. Cheeseman, G. Scalmani, V. Barone, B. Mennucci, G. A. Petersson, H. Nakatsuji, M. Caricato, X. Li, H. P. Hratchian, A. F. Izmaylov, J. Bloino, G. Zheng, J. L. Sonnenberg, M. Hada, M. Ehara, K. Toyota, R. Fukuda, J. Hasegawa, M. Ishida, T. Nakajima, Y. Honda, O. Kitao, H. Nakai, T. Vreven, J. A. Montgomery, J. E. Peralta, F. Ogliaro, M. Bearpark, J. J. Heyd, E. Brothers, K. N. Kudin, V. N. Staroverov, R. Kobayashi, J. Normand, K. Raghavachari, P. G. Rendell, J. C. Burant, S. S. Iyengar, J. Tomasi, M. Cossi, N. Rega, J. M. Millam, M. Klene, J. E. Knox, J. B. Cross, V. Bakken, C. Adamo, J. Jaramillo, R. Gomperts, R. E. Stratmann, O. Yazyev, A. J. Austin, R. Cammi, C. Pomelli, J. W. Ochterski, R. L. Martin, K. Morokuma, V. G. Zakrzewski, G. A. Voth, P. Salvador, J. J. Dannenberg, S. Dapprich, A. D. Daniels, O. Farkas, J. B. Foresman, J. V. Ortiz, J. Cioslowski, D. J. Fox, Gaussian 09, Revision D.01 (Gaussian Inc., 2009).

55. SDBSWeb (National Institute of Advanced Industrial Science and Technology, 2022); http://sdbs.db.aist.go.jp.

56. H. Dahn, P. Péchy, Concerning the chemical shift data (^{17}O, ^{13}C, ^{1}H) of formaldehyde. *Magn. Reson. Chem.* **34**, 723–724 (1996).